Int J Coal Sci Technol (2021) 8(5):938–955
https://doi.org/10.1007/s40789-020-00390-5

Characteristics of evolution of mining-induced stress field in the longwall panel: insights from physical modeling

Jinfu Lou[1,2] · Fuqiang Gao[1,2] · Jinghe Yang[1,2] · Yanfang Ren[1,2] · Jianzhong Li[1,2] · Xiaoqing Wang[2] · Lei Yang[1,2]

Received: 11 July 2020 / Revised: 30 September 2020 / Accepted: 3 December 2020 / Published online: 27 January 2021

Abstract The evolution of mining-induced stress field in longwall panel is closely related to the fracture field and the breaking characteristics of strata. Few laboratory experiments have been conducted to investigate the stress field. This study investigated its evolution by constructing a large-scale physical model according to the in situ conditions of the longwall panel. Theoretical analysis was used to reveal the mechanism of stress distribution in the overburden. The modelling results showed that: (1) The major principal stress field is arch-shaped, and the strata overlying both the solid zones and gob constitute a series of coordinated load-bearing structures. The stress increasing zone is like a macro stress arch. High stress is especially concentrated on both shoulders of the arch-shaped structure. The stress concentration of the solid zone in front of the gob is higher than the rear solid zone. (2) The characteristics of the vertical stress field in different regions are significantly different. Stress decreases in the zone above the gob and increases in solid zones on both sides of it. The mechanical analysis show that for a given stratum, the trajectories of principal stress are arch-shaped or inversely-arched, referred to as the "principal stress arch", irrespective of its initial breaking or periodic breaking, and determines the fracture morphology. That is, the trajectories of tensile principal stress are inversely arched before the first breaking of the strata, and cause the breaking lines to resemble an inverted funnel. In case of periodic breaking, the breaking line forms an obtuse angle with the advancing direction of the panel. Good agreement was obtained between the results of physical modeling and the theoretical analysis.

Keywords Longwall mining · Mining-induced stress field · Physical modeling · Principal stress trajectory · Strain brick

1 Introduction

Longwall mining has been widely used in China for nearly half a century (Kang et al. 2019b; Wang 2018; Xu et al. 2004). Owing to such outstanding technical advantages as a high level of mechanization, high annual output, and high recovery rate, it has become the technique of choice in most underground coal mines (Wang 2014). In terms of safe and efficient mining of thick or ultra-thick coal seams in particular, the large-height fully mechanized mining (LHM) or top coal caving (TCC) method has proven to be the most efficient technologies (Wang et al. 2014, 2015a; Yu et al. 2015).

The mining heights of the longwall panels have been increasing in the past decade, with a large number of panels with cutting heights exceeding 6 m (Ju and Xu 2013; Wang and Pang 2017). The maximum cutting height of LHM has reached 8.5 m in China, the rated working resistance of ZY26000/40/88D hydraulic supports is 26,000 kN, and the annual output of a single panel is up to 16 Mt. The cutting height of TCC is up to 5.0 m, the top coal caving height is 10–15 m, and the annual output exceeds 10 Mt (Wang et al. 2015a).

✉ Jinfu Lou
loujinfu@tdkcsj.com

[1] Coal Mining Research Institute, China Coal Technology and Engineering Group Co., Ltd., Beijing 100013, China

[2] State Key Laboratory of Coal Mining and Clean Utilization (China Coal Research Institute), Beijing 100013, China

With the widespread application of the fully mechanized mining technologies, such as LHM and TCC, both the cutting height and the advancing velocity have increased rapidly, which implies an increase in the intensity of excavation of the longwall panel (Bai and Tu 2019; Bandyopadhyay et al. 2020). This can lead to such strata behaviors as coal wall spalling (Bai et al. 2016; Wang and Pang 2017), hydraulic support crushing disasters(Ju et al. 2015), and other accidents that endanger the safety of workers (Li et al. 2007; Qi et al. 2019).

Mining activities and accidents are mechanics-oriented problems (Galvin 2016; Kaiser 2019; Peng 2019; Qian and Xu 2019; Zhao et al. 2019; Zuo et al. 2019) that can be attributed to the stress redistribution in the overburden(Brady and Brown 2013; Galvin 2016; Song et al. 2020). The evolution of the mining-induced stress field is closely related to the distribution of mining-induced fracture field and macroscopic breaking characteristics of the strata (Bai and Tu 2019). It's vital to various mining engineering practices, such as the design of hydraulic supports (Lou et al. 2017; Singh and Singh 2010), roadway support (Kang 2014; Wang et al. 2016), process of coal pillar failure (Singh et al. 2011), caving of top coal (Le et al. 2017; Yasitli and Unver 2005), characteristics of gas migration (Guo and Yuan 2015; Li et al. 2014), and the prevention of accidents owing to inrushing water(Wang and Park 2003; Zhang and Shen 2004). That is, the evolution of mining-induced stress field is the fundamental reason of strata behaviors (Qian et al. 2010). Therefore, a good understanding of its distribution and evolution is a prerequisite for solving the above engineering problems because this can provide a sound theoretical basis for roof control and disaster prevention in longwall panels.

In the past few decades, extensive research has been conducted on distribution of the mining-induced stress in longwall panels. The most commonly used research methods include theoretical calculation (Rezaei et al. 2015; Wu et al. 2012; Xie et al. 2015; Yang and Xie 2010), numerical simulation(Gao et al. 2014; Guo et al. 2012; Islam et al. 2009; Wang et al. 2013), and field measurements(Kaiser et al. 2001; Kang et al. 2019a; Kelly et al. 2002; Sinha and Walton 2019; Wang et al. 2015b; Xia et al. 2011). Some consensus has been reached. In particular, the redistribution of the vertical stress in solid zone around the gob has been determined qualitatively (Peng 2019; Qian et al. 2010). Figure 1 illustrates an idealized distribution of the mining-induced vertical stress surrounding a longwall panel (Peng 2019). The advancing and lateral abutment pressures increase to their peak values at a certain distance from the panel, then decrease with increasing distance from the panel, and finally return to their original values.

Summarizing the available methods on mining-induced stress field, it is found that the field measurement were mainly used to monitor vertical stress, such as the advancing and lateral abutment pressures around the panel (Mark 1989; Mark and Gadde 2010; Mark and Mucho 1994; Singh et al. 2011; Xue et al. 2020). Due to limitations of testing methods and testing cost, few studies have measured stress in the overburden strata (Mark 1990). By contrast, theoretical calculations, especially numerical simulations, have proven to be important tools for analyzing mining-induced stress and predicting failure-related behavior of the overburden (Gao and Stead 2014; Gao et al. 2015; Jing 2003).

However, in view of the complexity of geomechanics of longwall panels, it is insufficient to rely on a single research method. A multi-path approach should instead be used involving the corroboration of the outcomes to reduce potential risk (Kelly et al. 2002). As an indispensable approach to longwall mining, physical modeling has played a critical role in determining the movement and breaking of the strata as well as ground subsidence (Bai et al. 2019; Ghabraie et al. 2015b; Kang et al. 2018). It is based on similarity theory, and the model is composed of similar materials with varying mixture schemes. The physical and mechanical properties of the model materials are naturally similar to rock mass in the field (Gao et al. 2019), and its boundary conditions are as similar as possible to the field conditions. The results of physical modeling are visible and reliable, and can reproduce or predict phenomena under specific geo-mining conditions. Over the last few decades, strata control theories have had a profound influence on stope control, including the voussoir beam model, key stratum theory, three-zone division of overlying strata, and O-X fracturing characteristics of the main roof. These theories have been verified through physical modeling experiments in China (Qian et al. 1994, 2003, 2010).

Despite the widespread application of physical modeling, few cases have considered the stress field in the longwall panel. That is mainly because the stress measurement in physical modeling is still lagging behind advanced displacement measurement technologies, such as 3D laser scanning, close-range photogrammetry, and digital speckle (Ghabraie et al. 2015a; Wang et al. 2009). Of the available stress-testing tools, embedded sensors remain the most commonly used. In most cases, miniature pressure sensors are used with shells made of metal or rubber, with deformation-related properties (Young's modulus) significantly different from the model materials (Liu et al. 2009a, b). These factors lead to poor deformation coupling and reduces the accuracy of testing results. With the development of fiber-optics grating in the past decade, FBG (Fiber Bragg Grating) strain sensors have been introduced into physical modeling to improve results (Li et al. 2016; Wang et al. 2012).

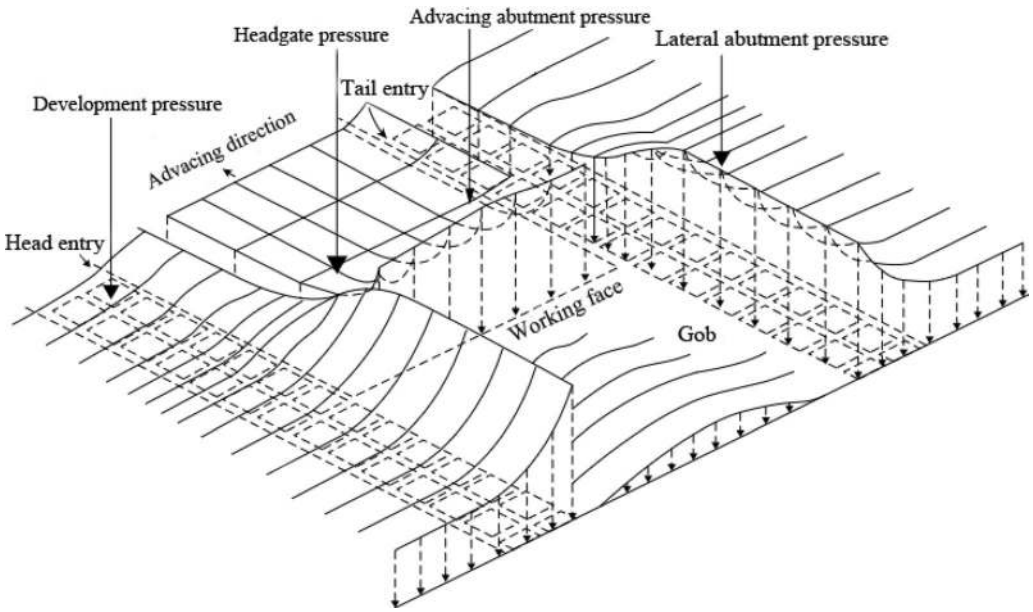

Fig. 1 Schematic of redistribution of vertical stress in a longwall panel (Peng 2019)

The simultaneous monitoring of the stress distribution and progressive breaking of the overburden can contribute to improving our understanding of the mechanism of breaking of the strata from the perspective of the evolution of stress. Moreover, this makes it possible to seek correlations between the mesoscopic mechanism of fracture propagation and the macroscopic breaking of the strata. This has engineering significance for stope management in longwall mining. This study proposed a system of physical modeling to carry out the real-time monitoring of mining-induced stress during model excavation to examine its distribution and evolution. Mechanical analysis was then used to reveal the mechanism of stress distribution as well as the correlation between the distribution of principal stress and the breaking of the strata.

2 Geo-mining conditions of the longwall panel

To ensure anonymity, the coal mine considered here was referred to as "Mine A". The W2302 panel of Mine A was considered as the prototype for the physical modeling. Located in a sub-horizontal coal seam with an average thickness of 6.2 m, W2302 panel was roughly 300 m wide, and the depth of the overburden was between 350 m and 430 m. The in situ stress measurement showed that the maximum horizontal principal stress varied from 13.1 to 17.89 MPa, with an average of 15 MPa, and was roughly parallel to the direction of excavation. The vertical stress varied from 11.55 to 13.76 MPa, with an average of 12.5 MPa.

W2302 panel was mined using the large-height longwall retreat mining method, and the average cutting height of coal was 6 m. The ZY12000/28/62 hydraulic support was used for stope control of the roof, the rated working resistance was 12,000 kN, and its shielding height varied from 2.8 to 6.2 m. The layout of the panel is shown in Fig. 2.

A generalized stratigraphic sequence of the overburden strata is shown in Fig. 4, compiled according to geological exploration boreholes. Note that the characteristics of strata have been combined with the physical model test scheme to avoid wordiness. The immediate roof was a 1.6-m-thick mudstone overlain by a 4.0-m-thick siltstone, which was the main roof. According to field observations, two fine sandstone strata were located at 7.73 m and 24.73 m above the coal seam, and were 6 m and 17 m thick, respectively. They had an important influence on both the breaking of the overlying strata and the stope control, and were called key stratum 1 (KS1) and key stratum 2 (KS2), respectively, in order to facilitate contextual references.

3 Configurations of the physical model

The experiment was conducted using a newly-developed physical modeling system designed for the large-scale modeling of longwall mining. It consists of a loading frame, a servo-control load module, a rotation positioning module, an integrated control platform, and a measuring system (Gao et al. 2019; Kang et al. 2018). The highly stiff, rotatable frame allows for maximum model dimensions of

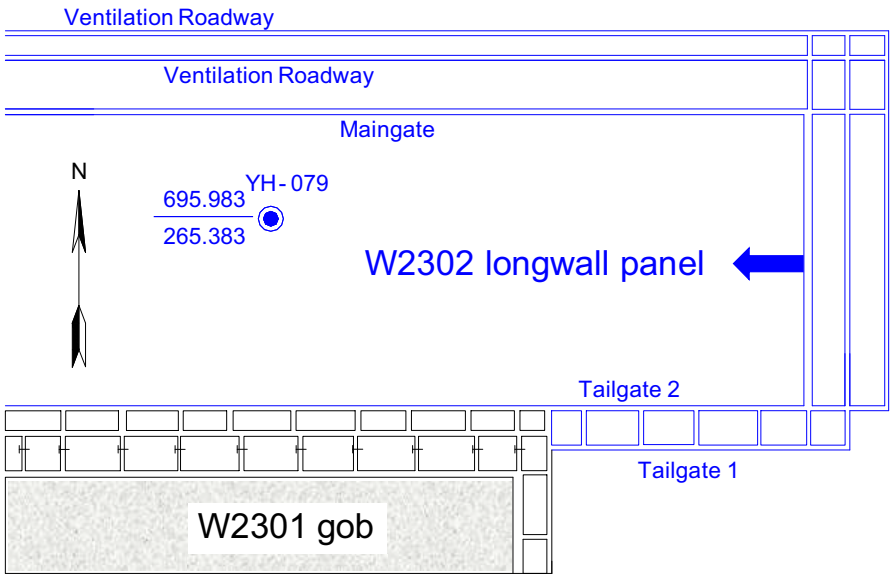

Fig. 2 The layout of W2302 longwall panel

5 m long, 2 m high, and 0.4 m thick to enable quasi-3D simulation conditions. Upon receiving the instruction signal from the integrated control platform, the servo-control load module can load in both the horizontal and vertical directions, respectively. Lateral gradient loads are achieved through four pairs of hydraulic cylinders on lateral sides of the frame to simulate in situ horizontal stress. The vertical loads are applied using 10 cylinders installed below the top beam, and each is separately loaded by a servo-control loop to achieve non-uniform vertical stress to compensate for undulating overburden. Using the rotation positioning module, the rotation angle of the frame can be varied from 0° to 60° to facilitate the construction of physical model with inclined strata. The physical modeling system and its scenario of application in this study are shown in Fig. 3.

As an indispensable part of the physical modeling system, the measuring system consists of a surface displacement scanning module, a stope supporting simulation module, and a mining-induced stress field module. In particular, the stress field module can be subdivided into three parts: abutment pressure module, internal stress module, and boundary stress module (see Sect. 4.1 for details).

The physical model was constructed according to the geological and mining conditions of W2302 panel. It is noted that in the physical modeling, the strength indices and densities of similar materials, geometric dimensions of the model, and time should follow the similarity theory (Ghabraie et al. 2015b):

$$\frac{C_\sigma}{C_\rho C_L} = 1, \quad C_t = C_L^{0.5}$$

where C_L is the constant of geometric similarity, C_σ is the constant of strength-related similarity, C_ρ is the constant of similarity in density between the prototype (full-scale case) and the model, and C_t is the constant of temporal similarity. They can be calculated as follows:

$$C_L = \frac{L_p}{L_m}, \quad C_\sigma = \frac{\sigma_p}{\sigma_m}, \quad C_\rho = \frac{\rho_p}{\rho_m}$$

where subscript p represents the prototype, m represents the model, L denotes length, σ represents strength, and ρ stands for bulk density.

In this study, C_L, C_ρ, C_σ, and C_t were 60, 1.39, 83.3, and 7.75, respectively.

The physical model had dimensions of 5 m × 1.85 m × 0.4 m along the X, Y and Z directions, respectively (see Figs. 3, 4). The model was constructed layer by layer, and had an average thickness of 30–50 mm. A total of five design schemes of similar materials were considered to simulate coal measures: coal seam, sandy mudstone, fine sandstone, siltstone and mudstone. The materials were constructed as a mixture of sand, gypsum, calcium carbonate, water and borax retarder. Different mixtures led to different strengths and extents of deformability. For each material, a trial-and-error procedure was used on small cylinder samples (50 mm in diameter, 100 mm high) until the target deformability and

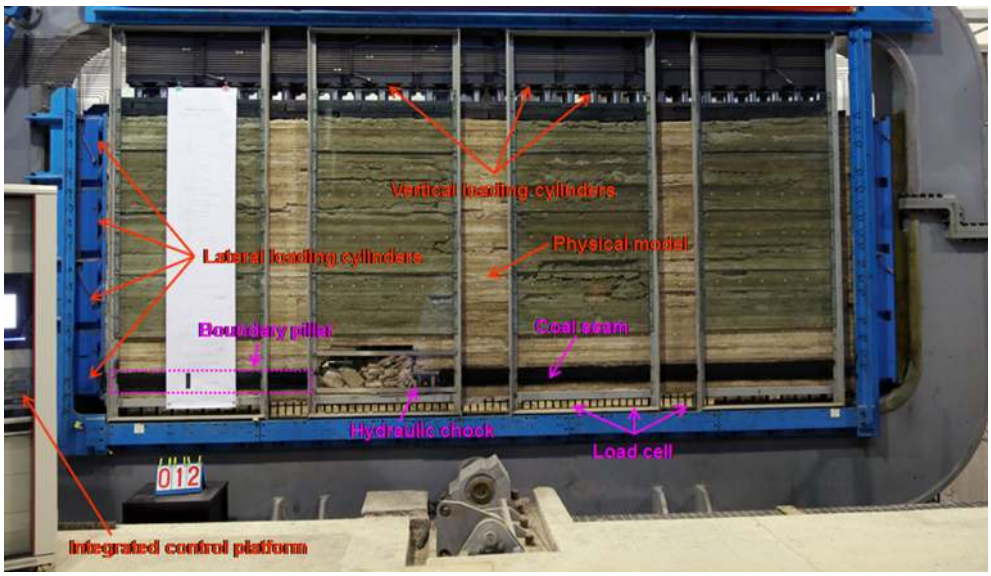

Fig. 3 Physical modeling system and application scenario

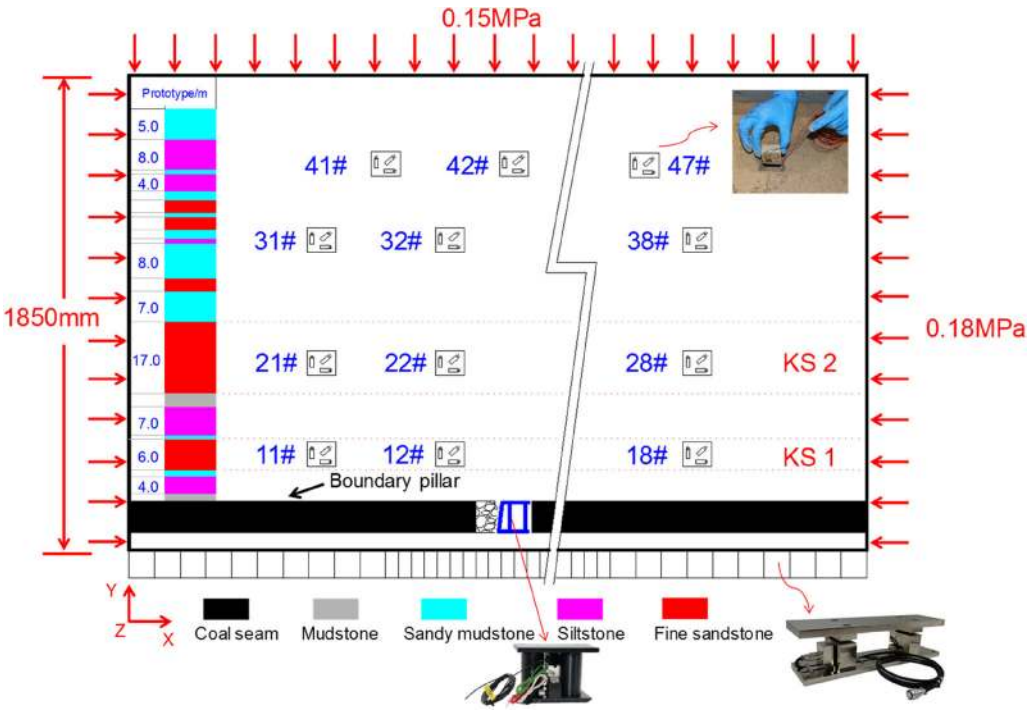

Fig. 4 Testing scheme of mining-induced stress field

strength were attained. The properties of the prototype rock sample and the corresponding mixture in the model are listed in Table 1.

Cross joints were incorporated by cutting each layer with a blade after it had been compacted by a vibrating device. Mica slices were placed between adjacent layers to simulate bedding planes. The entire model consumed about 8000 kg of raw materials, including 6129 kg of sand, 263 kg of high-strength gypsum, 63.5 kg of ordinary gypsum, 700 kg of calcium carbonate, 802 kg of water, and 8 kg of borax (retarders). It took six persons seven days to construct the model.

Table 1 Mechanical properties of prototype rock samples and similar materials

Lithology	Samples of intact rock				Target				Samples of physical model			
	UCS (MPa)	Tensile strength (MPa)	Young's modulus (GPa)	Poisson's ratio	UCS (kPa)	Tensile strength (kPa)	Young's modulus (MPa)	Poisson's ratio	UCS (kPa)	Tensile strength (kPa)	Young's modulus (MPa)	Poisson's ratio
Coal	21.97	1.29	3.93	0.31	440	26	79	0.31	698	64	187	0.12
Sandy mudstone	40.55	5.12	7.14	0.25	490	60	86	0.25	462	106	110	0.11
Fine sandstone	64.48	8.18	13.03	0.22	770	98	156	0.22	747	75	200	0.27
Siltstone	46.64	5.21	8.30	0.26	560	63	100	0.26	598	89	450	0.28
Mudstone	19.76	2.37	6.27	0.28	240	29	75	0.28	423	/	124	0.03

4 Testing scheme and excavation of physical model

4.1 Testing scheme for mining-induced stress field

The mining-induced stress field here was a combination of external boundary stress and internal stress of the model. The overall testing scheme was as follows: First, in different stages of excavation, the boundary stress on the top and lateral sides of the model were kept constant, and were determined by the servo-control load module. Stress along the bottom was measured by abutment pressure sensors. The stress distribution around the model boundary was thereby obtained. Second, the internal stress at different positions were obtained via the strain bricks embedded into the model, and then the stress distribution of the entire model could be achieved. The testing scheme is illustrated in Fig. 4.

4.1.1 Boundary stress module

As stated above, the vertical loading was realized by 10 hydraulic cylinders and horizontal loading by four pairs of lateral cylinders. These 14 servo load loops were controlled in real time by the integrated platform to maintain their respective constant outputs at a sampling frequency of 1 Hz. Data acquisition and post-processing were conducted automatically by the platform. The platform and operation interface are shown in Fig. 5.

4.1.2 Abutment pressure module

A total of 80 load cells were installed on the bottom beam of the frame to investigate the distribution of advancing abutment pressure. The prototype of the load cell is shown in Fig. 6. The vertical load applied to the load cell was transmitted to the database via the Strain Indicator and Recorder, and the results were displayed in real time. The results of calibration showed that the output was linear with respect to the applied load, and the load cell had high linearity, repeatability, and stable mechanical properties, as shown in Fig. 7. Its application in the physical modeling experiment is illustrated in Figs. 3 and 4.

4.1.3 Internal stress module

The strain brick was developed to test the internal stress of the model. During the construction of the model, pre-created strain bricks were buried in designated positions. During model excavation, the variation of strain bricks was transmitted to the database via the Strain Indicator and Recorder in real time. Unlike previous testing methods, the strain bricks were made of the same material as the simulated stratum where they were buried. Therefore, the strain bricks deformed in coordination with the model to realize the ideal coupling between them.

(1) Preparation of the strain brick

Each strain brick has dimensions of 40 mm × 40 mm × 20 mm, and the preparation process consists of forming a blank brick, sticking the foil strain gauge, moisture-proof treatment, and sand encapsulation. Considering that the moisture content of similar materials is about 8%–10% during model construction, the brick needs to be made moisture proof to prevent it from being soaked and softened. A composite moisture-proof solution was developed for this purpose and painted on the surface of the brick. It formed a thin film after hardening, whereby the brick would be coated. The moisture-proof treatment proved effective in the moisture resistance test. The preparation and application scenario are shown in Fig. 8.

To precisely determine the mechanical parameters of the brick, three groups of cylinder samples were formed using the same mixture as the bricks, each with a diameter of

(a) Integrated control platform (b) Operation interface

Fig. 5 The boundary stress module of the modeling system

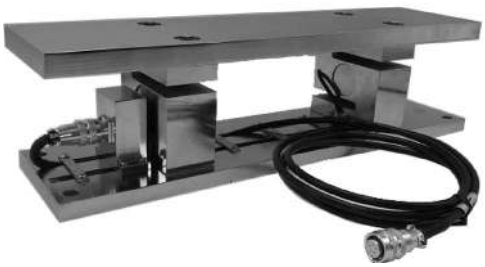

Fig. 6 Prototype of the load cell

50 mm, and with heights of 100, 50 and 25 mm, respectively. Such mechanical parameters as Young's modulus, UCS, shear strength, and Poisson's ratio were obtained and used for the stress calculation during model excavation. The testing scenario of the specimens is shown in Fig. 9.

(2) Internal stress-testing scheme

The stress distribution of the model was obtained by calculating the stress results of each brick and then using Kriging interpolation. To obtain the typical stress fields, such as vertical stress, horizontal stress and the principal stress, the three-element rectangular rosette was used, and the principal stress was obtained by calculating the components of strain at 0°, 45° and 90°. The prototype of strain brick is shown in Fig. 10.

According to the testing principle of three-element rectangular rosette, for any given strain brick, the principal stress on it can be calculated using the following equation (Dai et al. 2010):

$$\begin{cases} \sigma_1 = \dfrac{E}{2}\left[\dfrac{\varepsilon_0+\varepsilon_{90}}{1-\mu}+\dfrac{\sqrt{2}}{1+\mu}\sqrt{(\varepsilon_0-\varepsilon_{45})^2+(\varepsilon_{45}-\varepsilon_{90})^2}\right] \\ \sigma_3 = \dfrac{E}{2}\left[\dfrac{\varepsilon_0+\varepsilon_{90}}{1-\mu}-\dfrac{\sqrt{2}}{1+\mu}\sqrt{(\varepsilon_0-\varepsilon_{45})^2+(\varepsilon_{45}-\varepsilon_{90})^2}\right] \end{cases} \quad (1)$$

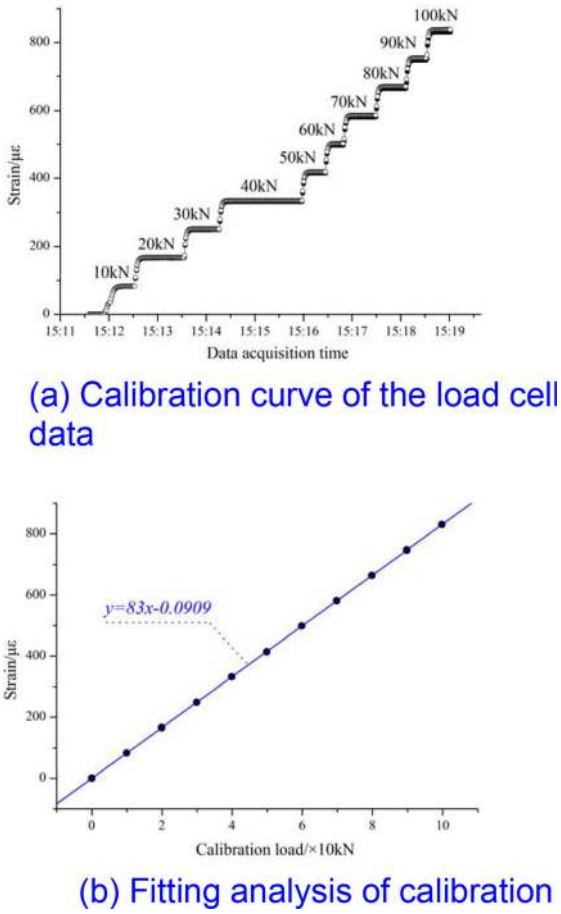

(a) Calibration curve of the load cell data

(b) Fitting analysis of calibration

Fig. 7 Loading responses of the load cell

where, E is the Young's modulus of the brick; μ is Poisson's ratio; ε_0, ε_{45} and ε_{90} are components of strain at 0°, 45° and 90°, respectively.

(a)Preparation of strain brick

(b) Moisture resistance test

(c) Application to the model

Fig. 8 Preparation and application of the strain brick

(a) UCS test (b) Shear strength test

Fig. 9 Mechanical properties test of the samples

The internal stress was measured by using four monitoring lines arranged in the model, numbered 1 #, 2 #, 3 #, and 4 # from bottom to top, and the spacing between adjacent bricks was about 500 mm. A total of 31 strain bricks were used, as shown in Fig. 4.

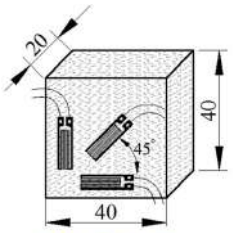

(a) Design scheme

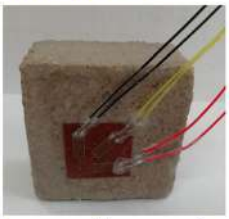

(b) Prototype with a rectangular rosette

Fig. 10 Schematic and prototype of the strain brick

4.2 Excavation of physical model

The experiment was conducted three months after construction to ensure that the model had dried out. In the experiment, longwall mining activity was simulated via model excavation. Prior to this, the boundary of the model was loaded by the servo-control load module to simulate the in situ stress field. A lateral stress of 0.18 MPa was applied via lateral hydraulic cylinders, corresponding to the in situ horizontal stress of 15 MPa (the stress similarity constant C_σ was 83.3), and a vertical stress of 0.15 MPa was applied by the top cylinders, corresponding to 12.5 MPa. Horizontal stress gradient was not considered in this physical model. All outputs of the cylinders were kept constant during the subsequent excavation stages.

To eliminate the influence of the boundary effect, a 1.3-m-wide boundary pillar was retained as the starting line for excavation based on theoretical calculations. The excavation began with a 200 mm cut in the coal seam (see Figs. 3, 4). Four house-made hydraulic chocks were then installed to simulate real hydraulic supports. Due to their characteristics of high linearity and repeatability, the hydraulic chocks have exhibited stable mechanical properties in previous physical modeling experiments (Kang et al. 2018; Lou et al. 2017), and can be used to simulate the working characteristics of the prototype supports. Longwall mining simulation was then performed stage by stage. A 50-mm-wide section was removed from the simulated coal seam in each stage. According to the constant of temporal similarity, we then waited 30 min before the next excavation, which corresponded to an advancing distance of 3 m in four hours. A total of 38 excavation stages were conducted continuously, and the total excavation width was 190 cm, equivalent to a real advancing distance of 114 m.

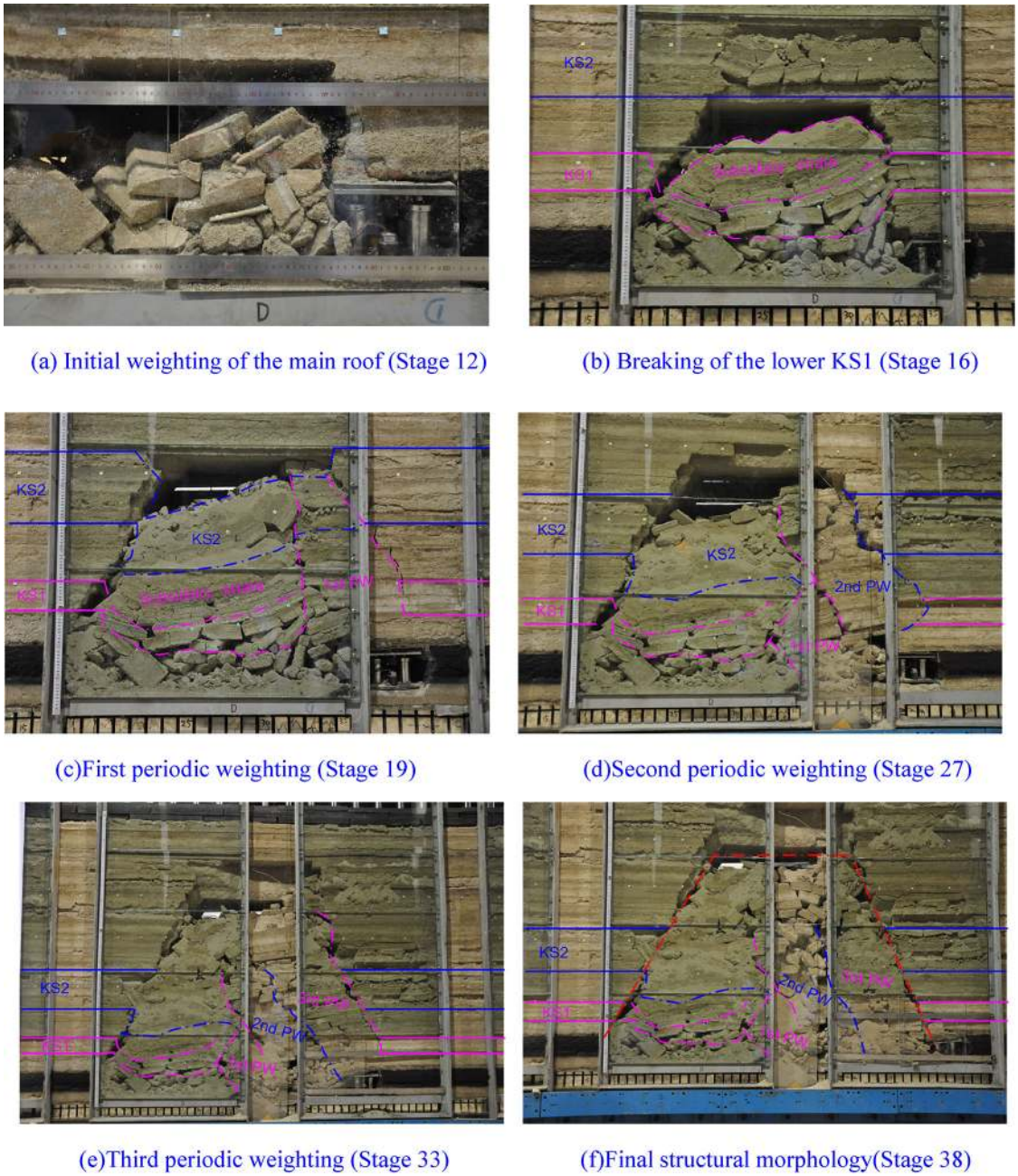

Fig. 11 Typical caving scenarios in different excavation stages. *PW* periodic weighting, KS1, KS2 key strata 1 and 2, respectively

5 Modeling results and comparison with field data

During model excavation, the overlying strata broke and caved successively, and the following typical stages of caving were observed: the breaking of immediate roof, the initial weighting, and three subsequent periodic weightings of the main roof. Typical caving scenarios are shown in Fig. 11. When the model was excavated towards the right, the individual strata had roughly the same breaking characteristics, i.e., the boundaries of breaking exhibited an approximately symmetrical "/\" outlines after the initial breaking, similar to an inverted funnel. In the three subsequent periodic breaks, the strata behaved like a cantilever beam, and the newly generated breaking line presented a "\"-shaped oblique outline. The mechanism of occurrence was interpreted using mechanical analysis in Sect. 7.

To verify the modeling results, the monitoring results, such as the steps of overburden breaking, the advancing abutment pressure, and working resistance of hydraulic chocks in the model were compared with the field observations. The physical model was found to be in good agreement with the field data. Taking the break of

Table 2 Comparison of modeling results with field observations

Excavation stage	Advancing distance (cm)	Equivalent distance (m)	Caving descriptions	Physical modeling versus field results
7	35	21	Caving of immediate roof	21 m versus 15 m
9	45	27	Caving of immediate roof	27 m versus 21 m
12	60	36	Initial weighting of main roof	36 m versus 32–37.4 m
16	80	48	Caving of KS1	12 m versus 13.7–15.4 m
19	95	57	First periodic weighting	9 m versus 13.7–15.4 m
27	135	81	Second periodic weighting	24 m versus 13.7–15.4 m
33	165	99	Third periodic weighting	18 m versus 13.7–15.4 m

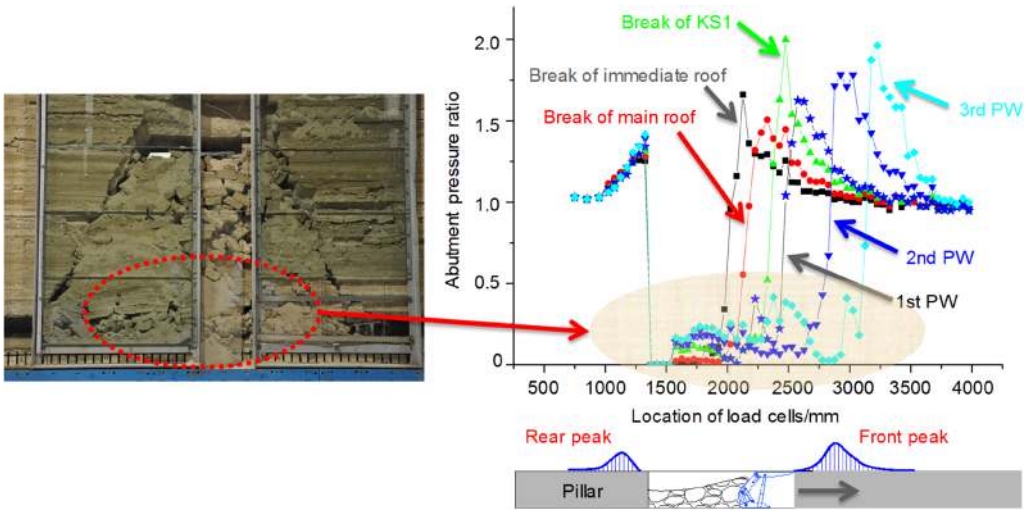

Fig. 12 Evolution of abutment pressure in different stages

overlying strata as an example, the immediate roof caved by 15–21 m compared with the modeling result of 21–27 m (geometric similarity constant, 60). Similarly, the initial weighting of the main roof was 32–37.4 m, and the modeling result was 36 m. The average step of periodic weighting of the main roof was 13.7–15.4 m, compared with the modeling results of 12 m, 9 m, 24 m and 18 m, as listed in Table 2.

6 Evolution of mining-induced stress field

According to the testing scheme in Sect. 4, the data needed for the stress field consisted of the physical quantities obtained from three testing devices: Hydraulic cylinders on the top and lateral sides (in units of MPa), load cells at the bottom (kN), and strain bricks embedded in the model ($\mu\varepsilon$), each of which had different physical dimensions. To compare the data in different stages, dimensionless analysis was used. For a given excavation stage, the three types of testing data were first calculated separately, and then compared with their respective initial values before excavation. Therefore, the data for each point was converted into a dimensionless ratio that reflected the degree of stress concentration. By calculating the stress ratios of all measuring points and utilizing the mathematical interpolation algorithm, the stress field in each stage was obtained.

6.1 Evolution of abutment pressure

A total of 80 load cells were used to measure the abutment pressure at the bottom boundary. Using dimensionless analysis, the distribution of abutment pressure in the typical stages of strata caving is shown in Fig. 12. It is clear that the abutment pressure featured two peaks, located in the retained pillar and the front solid zone, respectively. The magnitude of the rear peak varied from 1.26 to 1.42. By contrast, that of the front peak varied from 1.51 to 2, and its position and range of influence moved forward with model excavation. With increasing excavation width, the caving blocks in the gob were gradually compacted, and the values for the load cells located in the gob gradually rose.

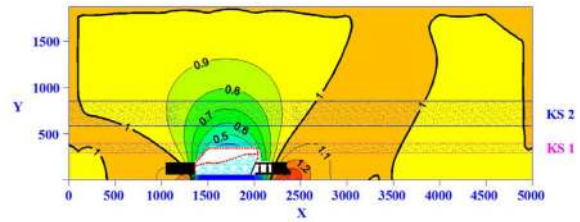

(a) Initial weighting of the main roof (Stage 12)

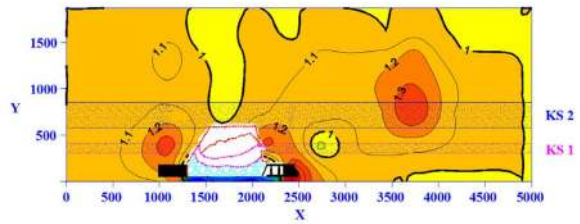

(b) Breaking of the lower KS1 (Stage 16)

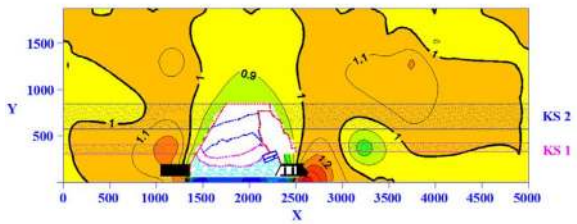

(c)First periodic weighting (Stage 19)

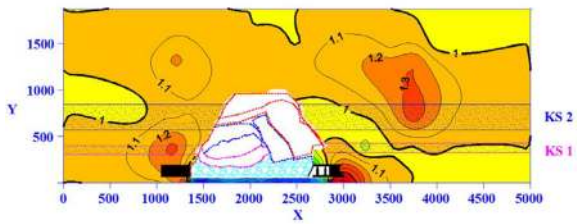

(d)Second periodic weighting (Stage 27)

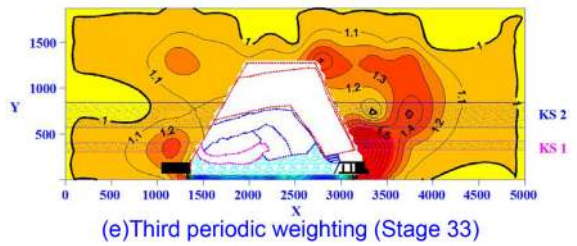

(e)Third periodic weighting (Stage 33)

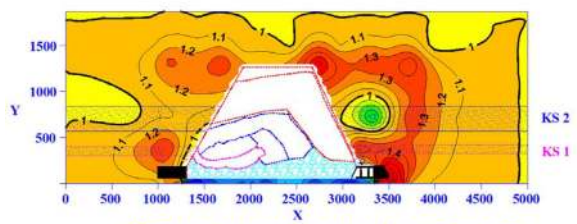

(f)Final structural morphology (Stage 38)

Fig. 13 Evolution of mining-induced major principal stress field

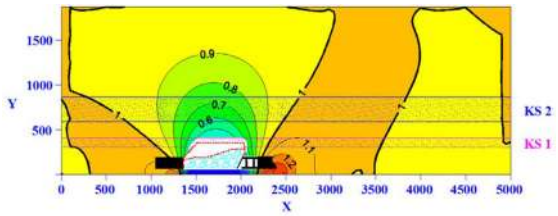

(a) Initial weighting of main roof (Stage 12)

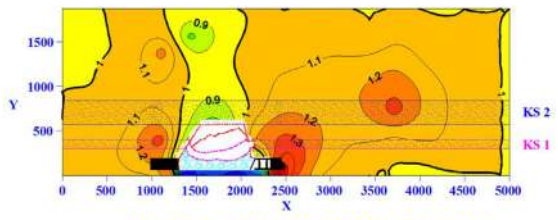

(b) Break of the lower KS1 (Stage 16)

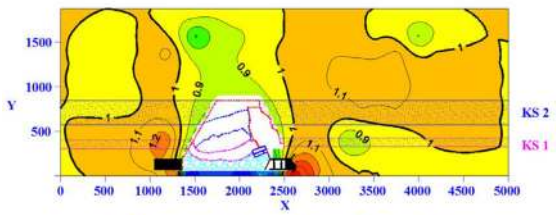

(c)1st periodic weighting (Stage 19)

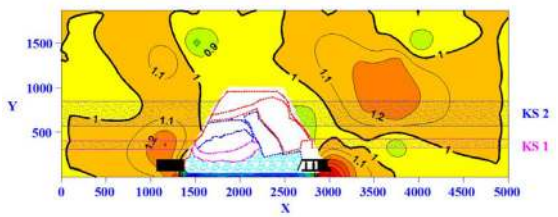

(d)2nd periodic weighting (Stage 27)

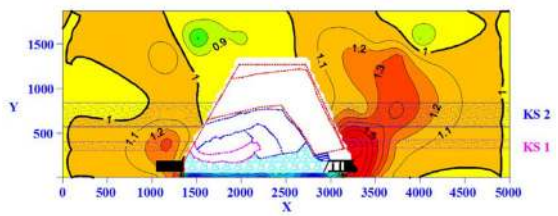

(e)3rd periodic weighting (Stage 33)

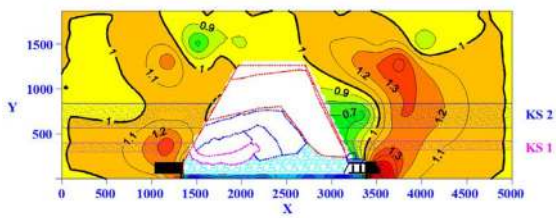

(f)Final structural morphology (Stage 38)

Fig. 14 Evolution of mining-induced vertical stress field

6.2 Evolution of principal stress field

It's widely accepted that the block structure formed after the fracture of overlying strata has a good bearing effect, and under this protection, the ground pressure in the panel is significantly relieved. Originating from the breaking of the strata and rearrangement of blocks, the block structure can be attributed to the evolution of mining-induced stress. According to the maximum normal stress criterion in the mechanics of materials, failure occurs if the maximum normal stress exceeds the ultimate tensile stress of the material, where this holds especially for brittle materials such as rocks. In longwall mining activities, the major principal stress (compressive stress) is related to the bearing characteristics of the strata while the minor principal stress (tensile stress) is closely related to their breaking process.

By combining the principal stress at the boundaries of the model and test data from the strain bricks (see "Appendix" for details), the major principal stress field in different stages is shown in Fig. 13. It was noted that with the increase in excavation width and the range of caving, the major principal stress field evolved from a zonal distribution to a macro-arch. The typical stages of evolution were as follows:

(1) In the early stages, with the caving of the lower strata, the upper strata above the gob was characterized by reduced major principal stress while the strata above the solid zone featured increasing principal stress. The outlines of the border of the former were similar to a funnel, the stress contours were arch-shaped, and the magnitude varied from 0.5 to 1.0.

(2) As excavation width increased, especially after the breaking and caving of thick strata, such as the main roof and KS1, the borders of the stress reduction zone converged towards the gob. The zone of increasing stress gradually expanded towards the upper strata above the gob. The range of influence of the advancing abutment pressure was constantly increasing, and the ratio varied from 1.1 to 1.3.

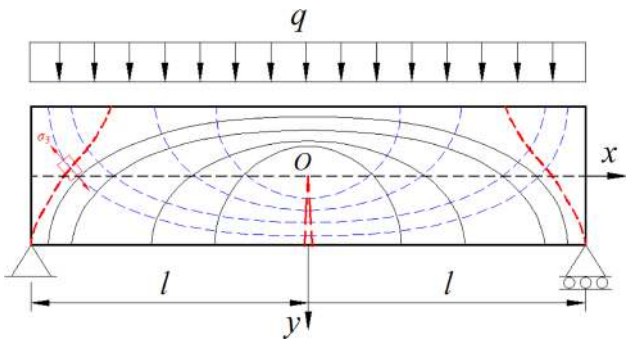

Fig. 15 Trajectories of principal stress before the initial breaking of the stratum

(3) With further expansion of the caved zone, the upper strata overlying both the solid zones and the gob formed a coordinated bearing structure. The zone of increasing stress was like a macro-arch. High stress was concentrated on both shoulders of the arch-shaped structure. The stress concentration in the front solid zone was higher than in the rear solid zone, with ranges of variation of 1.1–1.3 and 1.4–1.6, respectively.

We attempted to determine the evolution of the minor principal stress field, which, after all, was closely related to the breaking of the strata. However, the variation in the minor principal stress in almost all strain bricks was so small that there was no significant difference in different stages. This might be attributed to the following:

(1) The stress state of the overburden was mainly compressive, because of which the variation in the minor principal stress (tensile stress) was not significant, which was confirmed by the test data.

(2) The physical model was made of brittle materials. That was, compared with compressive strength, its tensile strength was much lower. Once a certain position was dominated by tensile stress, crack initiation was likely, immediately followed by the relevant stratum caving. As a consequence, the associated strain brick fell into the gob, and the test data instantly dropped to zero. In view of the fact that the gob was compacted by discrete blocks, the test data from these falling strain bricks were no longer applicable to the interpolation of the stress field. That was, the testing period of each strain brick usually ended with its falling, because of which the test data changed little.

6.3 Evolution of vertical stress field

As illustrated in Fig. 14, it's evident that the vertical stress field featured zonal evolution. The zone of a reduction in vertical stress was above the gob, and its magnitude was between 0.5 and 0.9. Stress increased in the solid zone on both sides, and the magnitude was between 1.1 and 1.7. The magnitude of the front zone was larger than that of the rear zone.

7 Discussion

The above has showed that the mining-induced principal stress field in the overlying strata was arch-shaped. In this section, a mechanical analysis is reported to examine its mechanism of distribution, followed by the drawing of a

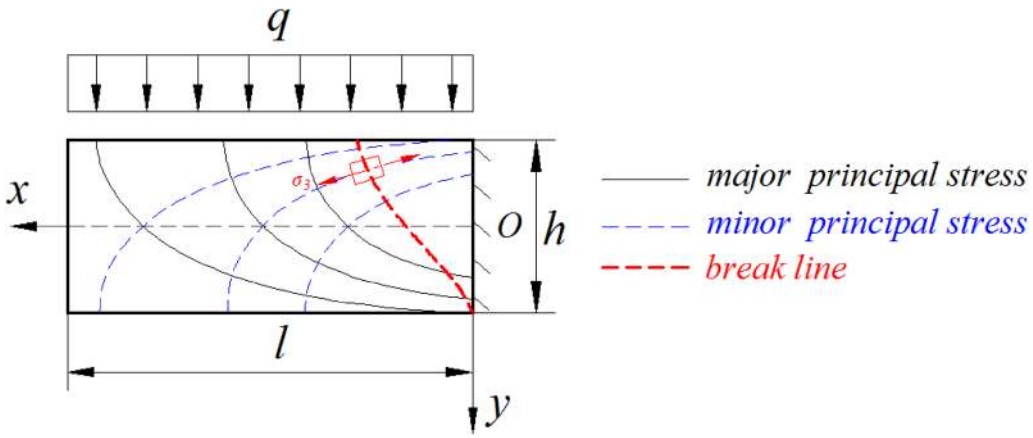

Fig. 16 Trajectories of principal stress before the periodic breaking of the stratum

correlation between the stress distribution and the breaking of the stratum.

7.1 Distribution mechanism of mining-induced principal stress field

The necessary simplifications were made before the mechanical analysis. First, the external load to which the stratum was subjected was simplified. It's widely known that coal measures are mainly composed of layered sedimentary strata. Any stratum of the overburden, therefore, is a "sandwich" clamped by adjacent strata (Qian et al. 2010). For simplicity, the load resulting from the upper and lower strata was treated as uniform, and acted uniformly on its top face (Zuo et al. 2017). Second, the model of the structure after the breaking of the overburden was simplified. Previous studies have shown that the overlying strata might be considered as a Kirchhoff plate that lies on a Winkler elastic foundation (Zhu and Qian 1987). The middle part of longwall panel could be further simplified into a semi-infinite long beam on a Winkler elastic foundation and analyzed as a plane strain problem (Qian et al. 2010). The breaking strata and structure of the blocks, accordingly, were considered as a beam model, such as the Voussoir beam model (Qian et al. 2010). Based on these two simplifications, the mining-induced stress analysis of the overburden was found to be equivalent to the response of a beam under uniform load.

7.1.1 Distribution of principal stress upon the first breaking of rock stratum

The initial load conditions of any overlying stratum can be regarded as a beam model under uniform load (see Fig. 15). According to the theory of elasticity (Gere and Goodno 2009), the variation of principal stresses throughout this rectangular beam can be represented by two systems of orthogonal curves: trajectories of the principal stress that give the directions of the principal stresses, as shown in Fig. 15. The curves for major and minor principal stresses always intersect at right angles, and every trajectory crosses the longitudinal axis at 45°. On the top and bottom surfaces of the beam, where shear stress is zero, the trajectories are either horizontal or vertical.

As is evident from Fig. 15, the trajectories of the major principal stress, i.e., compressive principal stresses, are arch-shaped; by contrast, those of the minor principal stress, i.e., tensile principal stresses, are inversely-arched. By comparing Figs. 13 and 15, it is clear that in terms of the distribution of compressive principal stresses, both demonstrate an outline of the "principal stress arch". The experimental results are in good agreement with the theoretical analysis, thus verifying the reliability of the physical modeling.

7.1.2 Distribution of principal stress at the periodic breaking of rock stratum

Similarly, according to the load conditions before periodic weighting, the rock stratum can be considered as a cantilever beam, and the distribution of trajectories is illustrated in Fig. 16. The distribution in Fig. 16 is exactly opposite to that in Fig. 15. It's clear that the compressive principal stresses are inversely-arched while the minor principal stresses are arch-shaped.

7.1.3 Formation mechanism of "principal stress arch"

The above analysis shows that for a given stratum of the overburden, irrespective of its initial breaking or periodic breaking, the trajectories of principal stress are arch-shaped or inversely-arched, which is verified by the above modeling results to a large extent. The formation mechanism of the "principal stress arch" can be interpreted with

reference to the theories of soil mechanics and tunneling engineering (Terzaghi 1996). As is well known, the stress state of the overburden was altered due to longwall mining activities. During the strata movement, the path of load transfer deviated to resist deformation, which resulted in a deflection in the principle stress such that the stress trajectories were arranged in an orderly manner, showing an arched shape. Therefore, the rock materials spontaneously adjusted themselves to achieve stability in response to the altering stress conditions, similar to the mechanism of the "pressure arch effect" in soil excavation and tunneling engineering (Kovari 1994).

7.2 Correlation between principal stress distribution and breaking of stratum

It is widely accepted that mining-induced stress is closely related to the micro-fracture initiation, propagation, coalescence until macro-failure occurs in the stratum. This study used the maximum normal stress criterion, which is applicable to the failure of brittle materials, to predict the failure characteristics of the stratum. According to this failure criterion, tensile principal stress is the decisive factor in the fracture of brittle materials, and the stratum accordingly breaks along the direction perpendicular to the trajectories of minor principal stress (Zuo et al. 2017). Taking the first breaking of the stratum as an example, as indicated in Fig. 15, some inclined cracks first appeared in the upper tensile zone near both ends of the stratum and propagated downward, followed by vertical cracks initiating in the lower tensile zone of the midspan and propagating upward. The resulting failure mode is shown by the red dashed line in Fig. 15, where the breaking lines at both ends demonstrate approximately symmetrical "/\ " outlines. Similarly, as indicated in Fig. 16, it is easy to predict that the periodic fracture of the stratum might exhibit an inclined "\" shaped breaking line.

A comparison of the breaking lines of the strata in Figs. 11, 15 and 16 shows that good agreement was achieved between the results of physical modeling and those of theoretical analysis. That is, for a given stratum, the trajectories of tensile principal stress are inversely-arched before its first breaking, because of which the breaking lines resembles an inverted funnel. In case of periodic breaking, the breaking line forms an obtuse angle with the advancing direction of the panel, i.e., the breaking line is "\" shaped when the panel advances towards the right; by contrast, it is "/" shaped for the panel advancing towards the left. The distribution of trajectories of mining-induced principal stress determines the fracture morphology of the overburden. Therefore, this might be used to predict the breaking characteristics of the overlying strata.

8 Conclusions

Longwall mining activities disturb the original in situ stress equilibrium of the overburden. The mining-induced stress field, as a consequence, is closely related to various strata behaviors and potential dynamic disasters. In this study, the progressive evolution of mining-induced stress was investigated by means of a large-scale physical modeling experiment, and strain bricks were used to measure the stress in the model. Good agreement was achieved between field observations and results of the physical model in terms of the breaking steps of the strata, advancing abutment pressure, and working resistance of hydraulic chocks, indicating that the physical model captured the realistic response of overlying strata. The results were also consistent in terms of the distribution of principal stress and fracture morphology of the overburden.

A mechanical analysis showed that the trajectories of principal stress are arch-shaped or inversely-arched, referred to as "principal stress arch". This was verified by the experiment where the major principal stress field of the overburden was arch-shaped, the zone of increasing stress was like a macro-arch, and the strata overlying both the solid zones and the gob formed a coordinated bearing structure. For a given stratum, the trajectories of tensile principal stress were inversely-arched before its first breaking, and caused the breaking lines to resemble an inverted funnel. In case of periodic breaking, the breaking line formed an obtuse angle with the advancing direction of the panel. The vertical stress field featured zonal evolution.

Knowledge of the distribution of mining-induced stress and its correlation with the macroscopic fracture morphology of the overburden allows us to revisit the relevant strata behaviors from the viewpoint of stress evolution, so as to enhance the interpretation of disaster occurrence mechanism. Actually, the hard and thick overburden is widespread in many China coal mining areas, and a series of targeted countermeasures, such as the preconditioning of hard roofs, have been adopted to promote the regular collapse of strata. We believe a good understanding of mining-induced stress field is of great engineering significance for roof disaster prevention in longwall panel.

Acknowledgements This work was supported by the National Natural Science Foundation of China (NSFC, Grant No. 51874175) and the China Coal Technology & Engineering Group Foundation (Grant Nos. 2018RC001, KJ-2018-TDKCZL-02). Comments from two anonymous reviewers and the editor are also greatly appreciated.

Compliance with ethical standards

Conflict of interest There is no conflict of interest in preparation of this paper.

Appendix

See Tables 3 and 4.

Table 3 Statistics of major principal stress concentration coefficients of strain bricks

No. of strain brick	Excavation stage					
	Stage 12	Stage 16	Stage 19	Stage 27	Stage 33	Stage 38
1# monitoring line						
11#	1.08	1.14	1.11	1.14	1.16	1.19
12#	1.28	1.38	1.29	1.34	1.38	1.42
13#	0.80	/	/	/	/	/
14#	1.28	1.35	/	/	/	/
15#	/	/	/	/	/	/
16#	0.90	1.12	0.7	0.86	2.35	1.53
17#	1.02	1.13	1.01	0.97	1.21	1.32
18#	1.02	1.08	1.01	0.99	1.06	1.11
2# monitoring line						
21#	0.98	1.01	0.95	0.94	0.92	0.92
22#	1.05	1.11	1.07	1.08	1.05	1.08
23#	0.86	0.93	/	/	/	/
24#	1.09	1.08	/	/	/	/
25#	1.09	1.18	1.07	0.91	/	/
26#	1.07	1.15	1.04	1.03	0.93	0.50
27#	1.24	1.43	1.14	1.38	1.55	1.38
28#	1.05	1.09	1.03	1.09	1.13	1.11
3# monitoring line						
31#	1.03	1.04	1.03	1.06	1.07	1.07
32#	1.09	1.17	1.17	1.23	1.29	1.33
33#	0.96	0.97	0.92	1.06	1.19	1.37
34#	1.01	1.02	0.94	1.08	/	/
35#	/	/	/	/	/	/
36#	1.07	1.12	1.13	1.25	1.35	1.40
37#	1.16	1.26	1.22	1.30	1.37	1.49
38#	1.01	1.01	1.01	1.03	1.04	1.06
4# monitoring line						
41#	1.03	1.05	1.05	1.08	1.08	1.08
42#	0.96	0.94	0.93	1.08	1.11	1.13
43#	1.00	1.02	0.92	1.00	0.96	1.03
44#	0.99	0.99	0.98	0.99	0.96	0.97
45#	1.03	1.05	1.06	1.14	1.15	1.09
46#	1.00	1.00	1.00	1.05	1.09	1.14
47#	1.00	1.02	0.88	0.93	0.93	0.94
Minimum value	0.77	0.84	0.70	0.86	0.92	0.50
Maximum value	1.28	1.43	1.29	1.38	2.35	1.53

Once a strain brick falls into the gob, the test data thereafter is no longer applicable to the interpolation of stress field, and denoted as "/" in the table

Table 4 Statistics of vertical stress concentration coefficients of strain bricks

No. of strain brick	Excavation stage					
	Stage 12	Stage 16	Stage 19	Stage 27	Stage 33	Stage 38
1# monitoring line						
11#	1.06	1.12	1.09	1.11	1.13	1.15
12#	1.26	1.35	1.28	1.32	1.35	1.38
13#	0.38	/	/	/	/	/
14#	1.26	1.19	/	/	/	/
15#	/	/	/	/	/	/
16#	0.94	1.11	0.78	0.94	2.00	0.78
17#	0.97	1.06	0.91	0.82	1.18	1.29
18#	1.02	1.10	1.01	1.00	1.07	1.11
2# monitoring line						
21#	0.98	1.00	0.96	0.95	0.93	0.93
22#	1.02	1.08	1.03	1.04	1.01	1.03
23#	0.83	0.84	/	/	/	/
24#	1.08	1.02	/	/	/	/
25#	1.09	1.17	1.09	0.87	/	/
26#	1.08	1.19	1.10	1.19	1.13	0.65
27#	1.20	1.35	1.10	1.30	1.45	1.30
28#	1.08	1.13	1.05	1.13	1.20	1.22
3# monitoring line						
31#	1.00	1.01	0.98	1.02	1.04	1.02
32#	1.07	1.25	1.14	1.21	1.21	1.29
33#	0.93	0.93	0.89	0.96	1.00	1.04
34#	1.08	1.10	0.98	1.00	/	/
35#	/	/	/	/	/	/
36#	1.04	1.09	1.09	1.20	1.29	1.31
37#	1.11	1.16	1.13	1.24	1.34	1.47
38#	1.02	1.03	1.02	1.04	1.05	1.07
4# monitoring line						
41#	1.03	1.06	1.02	1.08	1.08	1.08
42#	0.85	0.76	0.67	0.76	0.67	0.64
43#	0.97	0.97	0.87	0.93	0.87	0.87
44#	1.00	1.00	1.00	1.00	0.97	0.97
45#	1.05	1.07	1.09	1.16	1.17	1.11
46#	0.99	1.00	0.98	1.01	1.03	1.06
47#	1.00	1.03	0.78	0.79	0.78	0.79
Minimum value	0.38	0.76	0.67	0.76	0.67	0.64
Maximum value	1.26	1.35	1.28	1.32	2.00	1.47

References

Bai Q, Tu S (2019) A general review on longwall mining-induced fractures in near-face regions. Geofluids 2019:1–22

Bai Q, Tu S, Chen M, Zhang C (2016) Numerical modeling of coal wall spall in a longwall face. Int J Rock Mech Min 88:242–253

Bai Q, Tu S, Wang F (2019) Characterizing the top coal cavability with hard stone band(s): insights from laboratory physical modeling. Rock Mech Rock Eng 52:1505–1521

Bandyopadhyay K, Mallik J, Ghosh T (2020) Dependence of fluid flow on cleat aperture distribution and aperture–length scaling: a case study from Gondwana coal seams of Raniganj Formation, Eastern India. Int J Coal Sci Technol 7(1):133–146

Brady BH, Brown ET (2013) Rock mechanics: for underground mining. Springer, Berlin

Dai F, Shen G, Xie H (2010) Experimental mechanics. Tsinghua University Press, Beijing

Galvin J (2016) Ground engineering-principles and practices for underground coal mining. Springer, Berlin

Gao F, Stead D (2014) The application of a modified Voronoi logic to brittle fracture modelling at the laboratory and field scale. Int J Rock Mech Min 68:1–14
Gao F, Stead D, Coggan J (2014) Evaluation of coal longwall caving characteristics using an innovative UDEC Trigon approach. Comput Geotech 55:448–460
Gao F, Stead D, Kang H (2015) Numerical simulation of squeezing failure in a coal mine roadway due to mining-induced stresses. Rock Mech Rock Eng 48:1635–1645
Gao F, Kang H, Lou J, Li J, Wang X (2019) Evolution of local mine stiffness with mining process: insight from physical and numerical modeling. Rock Mech Rock Eng 52:3947–3958
Gere J, Goodno B (2009) Mechanics of materials, 7th edn. Cengage Learning, Boston
Ghabraie B, Ren G, Smith J, Holden L (2015a) Application of 3D laser scanner, optical transducers and digital image processing techniques in physical modelling of mining-related strata movement. Int J Rock Mech Min 80:219–230
Ghabraie B, Ren G, Zhang X, Smith J (2015b) Physical modelling of subsidence from sequential extraction of partially overlapping longwall panels and study of substrata movement characteristics. Int J Coal Geol 140:71–83
Guo H, Yuan L (2015) An integrated approach to study of strata behaviour and gas flow dynamics and its application. Int J Coal Sci Technol 2:12–21
Guo H, Yuan L, Shen B, Qu Q, Xue J (2012) Mining-induced strata stress changes, fractures and gas flow dynamics in multi-seam longwall mining. Int J Rock Mech Min 54:129–139
Islam MR, Hayashi D, Kamruzzaman A (2009) Finite element modeling of stress distributions and problems for multi-slice longwall mining in Bangladesh, with special reference to the Barapukuria coal mine. Int J Coal Geol 78:91–109
Jing L (2003) A review of techniques, advances and outstanding issues in numerical modelling for rock mechanics and rock engineering. Int J Rock Mech Min 40:283–353
Ju J, Xu J (2013) Structural characteristics of key strata and strata behaviour of a fully mechanized longwall face with 7.0 m height chocks. Int J Rock Mech Min 58:46–54
Ju J, Xu J, Zhu W (2015) Longwall chock sudden closure incident below coal pillar of adjacent upper mined coal seam under shallow cover in the Shendong coalfield. Int J Rock Mech Min 77:192–201
Kaiser P (2019) From common to best practices in underground rock engineering. In: Rock mechanics for natural resources and infrastructure development-invited lectures: proceedings of the 14th international congress on rock mechanics and rock engineering (ISRM 2019), September 13–18, 2019, Foz do Iguassu, Brazil. CRC Press, pp 141–179
Kaiser P, Yazici S, Maloney S (2001) Mining-induced stress change and consequences of stress path on excavation stability—a case study. Int J Rock Mech Min 38:167–180
Kang H (2014) Support technologies for deep and complex roadways in underground coal mines: a review. Int J Coal Sci Technol 1:261–277
Kang H, Lou J, Gao F, Yang J, Li J (2018) A physical and numerical investigation of sudden massive roof collapse during longwall coal retreat mining. Int J Coal Geol 188:25–36
Kang H, Wu L, Gao F, Lv H, Li J (2019a) Field study on the load transfer mechanics associated with longwall coal retreat mining. Int J Rock Mech Min 124:1–10
Kang H, Xu G, Wang B, Wu Y, Jiang P, Pan J, Ren H, Zhang Y, Pang Y (2019b) Forty years development and prospects of underground coal mining and strata control technologies in China. J Min Strata Control Eng 1:8–40
Kelly M, Luo X, Craig S (2002) Integrating tools for longwall geomechanics assessment. Int J Rock Mech Min 39:661–676
Kovari K (1994) Erroneous concepts behind the New Austrian Tunnelling Method. Tunnels & Tunnelling 26:38–42
Le TD, Mitra R, Oh J, Hebblewhite B (2017) A review of cavability evaluation in longwall top coal caving. Int J Min Sci Techno 27:907–915
Li T, Cai M, Cai M (2007) A review of mining-induced seismicity in China. Int J Rock Mech Min 44:1149–1171
Li W, Cheng Y, Guo P, An F, Chen M (2014) The evolution of permeability and gas composition during remote protective longwall mining and stress-relief gas drainage: a case study of the underground Haishiwan Coal Mine. Geosci J 18:427–437
Li S, Liu H, Li L, Zhang Q, Wang K, Wang K (2016) Large scale three-dimensional seepage analysis model test and numerical simulation research on undersea tunnel. Appl Ocean Res 59:510–520
Liu H, Zhang J, Peng J (2009a) Full-scale model tests on behavior of cast-in-place concrete pipe piles with large diameter under lateral loads. Chin J Geotech Eng 31:161–165
Liu J, Zhao M, Yang M (2009b) Model tests on bridge pile foundation in high and steep rock slopes. Chin J Geotech Eng 31:372–377
Lou J, Kang H, Gao F, Yang J, Li J (2017) Determination of large-height support resistance based on multi-factor analysis. J China Coal Soc 42:2808–2816
Mark C (1989) Analysis of longwall pillar stability. The Pennsylvania State University, State College
Mark C (1990) Pillar design methods for longwall mining. US Department of the Interior, Bureau of Mines
Mark C, Gadde M (2010) Global trends in coal mine horizontal stress measurements. In: Aziz N, Kininmonth B (eds) Proceedings of the 2010 Coal Operators' Conference, Mining Engineering, University of Wollongong, 11–12 February 2010
Mark C, Mucho TP (1994) Longwall mine design for control of horizontal stress. US Bureau of Mines Special Publication 1994:01–94
Peng SS (2019) Longwall mining. CRC Press, Boca Raton
Qi Q, Li Y, Zhao S, Zhang N, Zheng W, Li H, Li H (2019) Seventy years development of coal mine rockburst in China: establishment and consideration of theory and technology system. Coal Sci Technol 47:1–40
Qian M, Xu J (2019) Behaviors of strata movement in coal mining. J China Coal Soc 44:973–984
Qian M, Miao X, He F (1994) Analysis of key block in the structure of voussoir beam in longwall mining. J China Coal Soc 19:557–563
Qian M, Miao X, Xu J, Mao X (2003) Study of key strata theory in ground control. China University of Mining and Technology Press, Xuzhou
Qian M, Shi P, Xu J (2010) Underground pressure and strata control. China University of Mining and Technology Press, Xuzhou
Rezaei M, Hossaini MF, Majdi A (2015) Determination of longwall mining-induced stress using the strain energy method. Rock Mech Rock Eng 48:2421–2433
Singh G, Singh U (2010) Prediction of caving behavior of strata and optimum rating of hydraulic powered support for longwall workings. Int J Rock Mech Min 47:1–16
Singh AK, Singh R, Maiti J, Kumar R, Mandal P (2011) Assessment of mining induced stress development over coal pillars during depillaring. Int J Rock Mech Min 48:805–818
Sinha S, Walton G (2019) Investigation of longwall headgate stress distribution with an emphasis on pillar behavior. Int J Rock Mech Min 121:1–13
Song Z, Ji H, Liu Z, Sun L (2020) Study on the critical stress threshold of weakly cemented sandstone damage based on the renormalization group method. Int J Coal Sci Technol. https://doi.org/10.1007/s40789-020-00315-2

Terzaghi K (1996) Theoretical soil mechanics, 3rd edn. Wiley, New York

Wang J (2014) Development and prospect on fully mechanized mining in Chinese coal mines. Int J Coal Sci Technol 1:253–260

Wang J (2018) Engineering practice and theoretical progress of top-coal caving mining technology in China. J China Coal Soc 43:43–51

Wang G, Pang Y (2017) Surrounding rock control theory and longwall mining technology innovation. Int J Coal Sci Technol 4:301–309

Wang J, Park H (2003) Coal mining above a confined aquifer. Int J Rock Mech Min 40:537–551

Wang H, Li S, Zheng X, Zhu W (2009) Research progress of geomechanical model test with new technology and its engineering application. Chin J Rock Mech Eng 28:2765–2771

Wang J, Li S, Sui Q, Zhang J, Chen X, Wang Z, Bai T, Shi B (2012) Study of FBG strain sensors based on similar materiel in zonal disintegration model test. J China Coal Soc 37:1570–1575

Wang H, Jiang Y, Zhao Y, Zhu J, Liu S (2013) Numerical investigation of the dynamic mechanical state of a coal pillar during longwall mining panel extraction. Rock Mech Rock Eng 46:1211–1221

Wang J, Yang S, Li Y, Wei L, Liu H (2014) Caving mechanisms of loose top-coal in longwall top-coal caving mining method. Int J Rock Mech Min 71:160–170

Wang J, Yu B, Kang H, Wang G, Mao D, Liang Y, Jiang P (2015a) Key technologies and equipment for a fully mechanized top-coal caving operation with a large mining height at ultra-thick coal seams. Int J Coal Sci Technol 2:97–161

Wang S, Mao D, Pan J, Chen J, Chen F, Lan H (2015b) Measurement on the whole process of abutment pressure evolution and microseismic activities at the lateral strata of goaf. J China Coal Soc 40:2772–2779

Wang H, Jiang Y, Xue S, Mao L, Lin Z, Deng D, Zhang D (2016) Influence of fault slip on mining-induced pressure and optimization of roadway support design in fault-influenced zone. J Rock Mech Geotech 8:660–671

Wu Y, Wang H, Xie P (2012) Analysis of surrounding rock macro stress arch shell of longwall face in steeply dipping seam mining. J China Coal Soc 37:559–564

Xia Y, Pan J, Wang Y, Zhang Y (2011) Study of rule of surrounding rock failure and stress distribution based on high-precision microseismic monitoring. J China Coal Soc 36:239–243

Xie S, Li S, Huang X (2015) Surrounding rock principal stress difference evolution law and control of gob-side entry driving in deep mine. J China Coal Soc 40:2355–2360

Xu J, Zhu W, Lai W, Qian M (2004) Green mining techniques in the coal mines of China. J Mines Met Fuels 52:395–398

Xue D, Zhou J, Liu Y, Gao L (2020) On the excavation-induced stress drop in damaged coal considering a coupled yield and failure criterion. Int J Coal Sci Technol 7(1):58–67

Yang K, Xie G (2010) Modeling and analyzing on the development of mining induced stress shell in deep longwall mining. J China Coal Soc 35:1066–1071

Yasitli N, Unver B (2005) 3D numerical modeling of longwall mining with top-coal caving. Int J Rock Mech Min 42:219–235

Yu B, Zhao J, Kuang T, Meng X (2015) In situ investigations into overburden failures of a super-thick coal seam for longwall top coal caving. Int J Rock Mech Min 78:155–162

Zhang J, Shen B (2004) Coal mining under aquifers in China: a case study. Int J Rock Mech Min 41:629–639

Zhao Y, Zhou H, Zhong J, Liu D (2019) Study on the relation between damage and permeability of sandstone at depth under cyclic loading. Int J Coal Sci Technol 6(4):479–492

Zhu D, Qian M (1987) The computer simulation of the main roof breaking of the longwall face. J China Univers Min Technol 1987:1–9

Zuo J, Sun Y, Qian M (2017) Movement mechanism and analogous hyperbola model of overlying strata with thick alluvium. J China Coal Soc 42:1372–1379

Zuo J, Wang J, Jiang Y (2019) Macro/meso failure behavior of surrounding rock in deep roadway and its control technology. Int J Coal Sci Technol 6(3):301–319